Knowledge Based Airfoil Aerodynamic and Aeroacoustic Design

B. Greschner[*], C. Yu[§], S. Zheng[§], M. Zhuang[§], Z. J. Wang[§] and F. Thiele[*]

[*]*Hermann-Foettinger-Institute of Fluid Mechanics*
Berlin University of Technology, Mueller-Breslau-Str. 8, D-10623 Berlin, Germany

[§]*Department of Mechanical Engineering*
Michigan State University, East Lansing, MI 48824

A systematic investigation of the unsteady flows around a series of NACA airfoils is carried out. The main objective is to conduct manual design case studies on the connections between an airfoil shape characteristics and its aerodynamic and aeroacoustic performance. The approach employs the unsteady CFD flow simulations in the near field of an airfoil and the FW-H integral method for the far field noise prediction. The work focuses on analyzing the aerodynamic and aeroacoustic performance of an airfoil and examining the sensitivities of the objective functions to various weighting factors. The results include identifying the optimum symmetric and asymmetric airfoils among the airfoils and suggesting the possible optimum airfoil characteristics. The results can be used to guide the selections of the geometric parameters and constraints in a fully automated aerodynamic and aeroacoustic optimization.

I. Introduction

Airfoil noise is caused mainly by the scattering of vortices into acoustic waves at the trailing edge and it is a major concern when addressing the noise generated by high-lift devices, fans, etc. In order to reduce the airfoil noise, some attempts to address aeroacoustics in the airfoil design process have been made in the recent years.[1-2] Similar to an aerodynamic shape optimization,[3-5] in a constrained aeroacoustic optimization, an airfoil shape can be expressed as a function of some design parameters. Ideally, the constrained aeroacoustic shape optimization could be performed by combining an optimizer with a CFD solver coupled with an automated grid generator and a sound propagation formula based on the Ffowcs Williams & Hawkings (FW-H) equation. A CFD simulation for the unsteady viscous flow in the immediate vicinity of an airfoil can be carried out in order to provide a reliable input to the FW-H equation for calculations of the far field noise. An optimizer would then evaluate hundreds or thousands of airfoil designs to achieve an optimum design with respect to both aerodynamic performance (through constraints) and aeroacoustic consideration. However this optimization process is cumbersome due to the fact that a high fidelity unsteady CFD simulation must also be performed hundreds or thousands of times while an optimum set of design parameters is being searched during an optimization. The airfoil parameterization methods that can accurately represent a variety of dramatically different airfoil shapes and can reflect subtle changes in local areas usually use a large number of design variables, so it would be very difficult to use such an approach due to an unrealistic demand on CPU time.

Instead of choosing a parameterization method and conducting a constrained aeroacoustic optimization (that could well be unrealistic), in the current work, we directly study the effects of an airfoil shape characteristics on its combined aerodynamic and aeroacoustic performance characteristics. In the study, a two-dimensional unsteady flow field around a series of 4-digit NACA airfoils is considered. Firstly, the unsteady viscous flow fields around the airfoils (symmetric and asymmetric) are calculated using a high fidelity CFD solver. The aerodynamic performance of the airfoils can then be evaluated. Secondly, the near field unsteady CFD solutions are used to calculate the far field noise using the FW-H equation. This hybrid method allows us to effectively evaluate the aeroacoustic performance of the airfoils. As a result of the systematic evaluations, a link between our knowledge on the overall performance and a variety of characteristics of an airfoil shape is established. In Sec. II, the details of the CFD code and the flow condition for the current study are described. The FW-H equation and the integral code verification are

American Institute of Aeronautics and Astronautics

given in Sec. III. In Sec. IV, the results of the effects of an airfoil shape on its aerodynamic and aeroacoustic performance are presented and analyzed. The conclusions are drawn in Sec. V.

II. CFD Solver and Flow Condition

A high fidelity in-house finite-volume based CFD code *ELAN*[6] is used for solving the unsteady Reynolds-averaged Navier-Stokes equations (RANS). The scheme is implicit and of second-order accuracy both in space and time. All scalar quantities as well as the Cartesian components of tensorial quantities are stored in the cell centers of arbitrarily curvilinear, semi-structured grids that can capture complex geometries and allow for local refinements. Diffusive terms are approximated with central schemes, whereas convective terms are treated with central or upwind-biased limited schemes of a higher order. The linearized equations are solved sequentially and the pressure is iterated to convergence using a pressure-correction scheme of the SIMPLE type. A generalized Rhie & Chow interpolation is used to avoid an odd-even decoupling of pressure, velocity and Reynolds-stress components. All computations are compressible using an equation for total thermal enthalpy and the ideal gas equation.

A systematic study of the flows around a series of NACA 4-digit airfoils (see Table 1) is carried out for the analysis of the aerodynamic and aeroacoustic performance of an airfoil. The freestream Mach number, M, is given as 0.2 with a turbulence intensity Tu = 1%. The chord length of the airfoil is $c = 0.3\,\mathrm{m}$ and the angle of attack is $\alpha =$ 20°. The reference values for the density, pressure and temperature are $\rho_0 = 1.162$ kg/m³, $p_0 = 100016$ Pa and $T_0 =$ 300 K respectively. The corresponding Reynolds number Re_c is about 1.4 million.

Table 1. The Selected NACA 4-Digit Airfoils

Symmetric cases	NACA 0006, NACA 0009, NACA 0012, NACA 0018, NACA 0024, NACA 0030
Asymmetric cases xx09	NACA 2409, NACA 4409, NACA 6309, NACA 6409, NACA 6609, NACA 8409
  xx12	NACA 2412, NACA 4412, NACA 6412, NACA 8312, NACA 8412, NACA 8612

An automated two-dimensional grid generator has been developed. The grid generation is based on algebraic algorithms with capabilities of handling complex geometry and resolving the boundary layer. The automatically generated grid around NACA 0012 airfoil is shown in Figure 1. The grid consists of eight blocks, depicted in Figure 2. The grid extends to $26c$ in the streamwise direction and $20c$ in the cross-stream direction. The two-dimensional
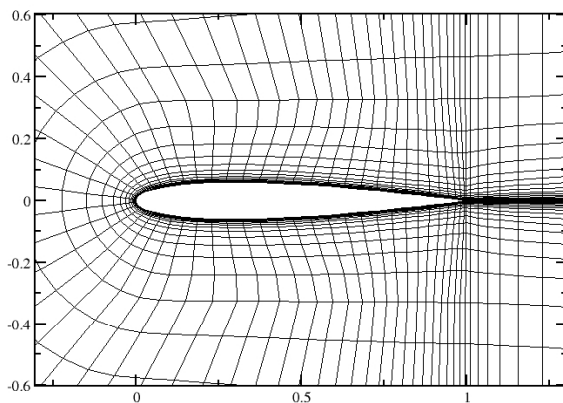

Figure 1. Grid for NACA0012 airfoil (zoomed in on the airfoil, every 4th grid point is shown).
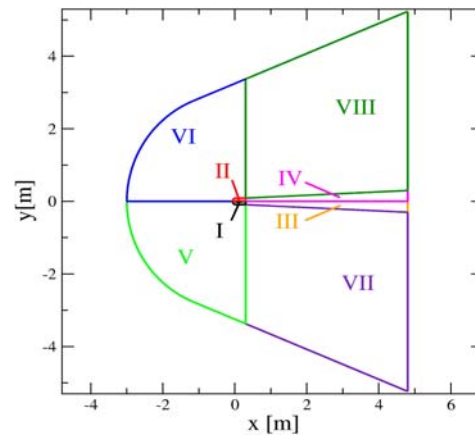

Figure 2. Complete grid dimension and related blocks of the grid.

grid is composed of about 50000 cells with 240 points on the airfoil surface in the circumferential direction. The grid is sufficiently fine to yield y^+ values of $1 < y^+ < 4$ in the leading edge region, except for the most critical airfoils, for which the y^+ values are up to $y^+ = 7$. The no-slip adiabatic condition is used at the airfoil surface. The left hand side boundaries (block V to VI) are defined as inlet and the right hand side boundaries (block III, IV & VII, VIII) are defined as outlet. The inflow and outflow conditions with a non-reflecting mode[7] are used at the inlet and outlet respectively. The time-step is given as $\Delta t = 1 \times 10^{-4}$ which leads to a minimum of 55 time-steps per period of the main perturbation frequency for every airfoil case. The number of time-steps computed for the unsteady statistics and acoustic output is 10000 and 4000, respectively. The unsteady RANS calculations are obtained using the two-equation LLR-k-ω model,[8] for which a universal high/low Reynolds number boundary condition[9] is used.

For the purpose of verification, numerical simulations of the flow around NACA0012 airfoil are carried out. A comparison of the pressure coefficient distribution on the airfoil surface between the simulation and the experiment[10] is shown in Figure 3 for the flow with the angle of attach $10°$ and Mach number $M = 0.2$. The surface pressure distribution and the calculated lift coefficient ($C_l = 0.894$) agree well with the experimental results. As the angle of attack is increased, the flow around the airfoil becomes unsteady and is characterized by a time dependent behavior of the separation region around the airfoil.
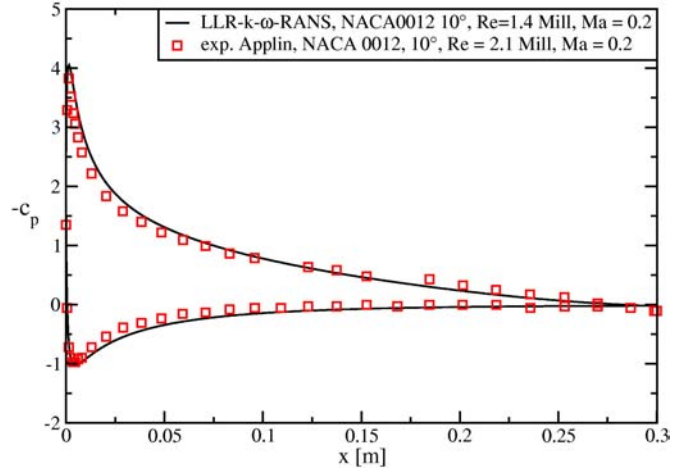

Figure 3. Comparison of the pressure coefficient distribution on the NACA 0012

III. The FW-H Equation

With the near field unsteady CFD solutions as an input, the far field sound pressure is predicted based on the FW-H equation. After the Galilean transformation, the FW-H equation can be written as

$$\left[\frac{\partial^2}{\partial t^2} + M_i M_j \frac{\partial^2}{\partial y_i \partial y_j} + 2M_i \frac{\partial^2}{\partial y_i \partial t} - \frac{\partial^2}{\partial y_i \partial y_i} \right] \left[H(f)p'(\mathbf{y},t) \right]$$

$$= \frac{\partial^2}{\partial y_i \partial y_j} [T_{ij} H(f)] - \frac{\partial}{\partial y_i} [F_i \delta(f)] + \frac{\partial}{\partial t} [Q\delta(f)]$$

(1)

with

$$T_{ij} = p\delta_{ij} + \rho u_i u_j - c_0^2 \rho' \delta_{ij}$$

$$F_i = \left(p\delta_{ij} + \rho(u_i - U_i)(u_j - U_j) + \rho_0 U_i U_j \right) \frac{\partial f}{\partial y_j}$$

$$Q = \left(\rho(u_i + U_i) - \rho_0 U_i \right) \frac{\partial f}{\partial y_i}$$

The term $p'(\mathbf{y},t)$ is the far field pressure perturbation. The terms, T_{ij}, F_i, Q, represent the contributions of quardrupole, dipole and monopole sources, respectively. The function $f = 0$ defines the FW-H surface, outside of which the acoustic solution is calculated. The variables, $u_i, -U_i$ and c_0, are the fluid velocities, the FW-H surface velocities and the speed of sound, respectively. The variables ρ, ρ_0 and ρ' represent the total density, the freestream density and the density perturbation on the FW-H surface, respectively.

The Kronecker delta, δ_{ij}, and the Heaviside function, $H(f)$, bear their common definitions. After the Fourier transform of the Eq. (1), the far field solution in the frequency domain can be calculated by[11]

$$p'(\mathbf{y},\omega) = -\oint_{f=0} i\omega Q(\xi,\omega) G(\mathbf{y};\xi) dl - \oint_{f=0} F_i(\xi,\omega) \frac{\partial G(\mathbf{y};\xi)}{\partial \xi_i} dl - \int_{f>0} T_{ij}(\xi,\omega) \frac{\partial^2 G(\mathbf{y};\xi)}{\partial \xi_i \partial \xi_j} d\xi$$

$$= p'_T(\mathbf{y},\omega) + p'_L(\mathbf{y},\omega) + p'_Q(\mathbf{y},\omega)$$

(2)

where ξ and $\mathbf{y}$ denote the co-ordinates of the two-dimensional source element and the far field observer locations respectively.

In the current study, the quadrupole term is neglected due to its small contributions. In order to verify the program code for solving the FW-H integral, the acoustic field from a monopole line source is computed by the code and compared with the analytical solution. Extending the original formulation given by Dowling and Ffowcs Williams,[12] the complex potential for a monopole source placed at the origin in a uniform flow with a given flow direction θ (see Figure 4) can be derived as

$$\Phi(x,y,t) = A \frac{i}{4\beta} \exp[i(\omega t + Mk\bar{x}/\beta^2)] H_0^{(2)}(\frac{k}{\beta^2}\sqrt{\bar{x}^2 + \beta^2 \bar{y}^2})$$ (3)

with
$$\begin{cases} \bar{x} = x\cos\theta + y\sin\theta \\ \bar{y} = -x\sin\theta + y\cos\theta \end{cases}$$

where M is the Mach number, k is the wave number defined by $k = \omega/c_0$, $\beta = \sqrt{1-M^2}$, and θ is the flow direction. The perturbation variables needed for the FW-H integral are obtained from

$$p' = -\rho_0\left(\frac{\partial\Phi}{\partial t} + U_0\frac{\partial\Phi}{\partial x} + V_0\frac{\partial\Phi}{\partial y}\right)$$

$$u' = \nabla\Phi$$ (4)
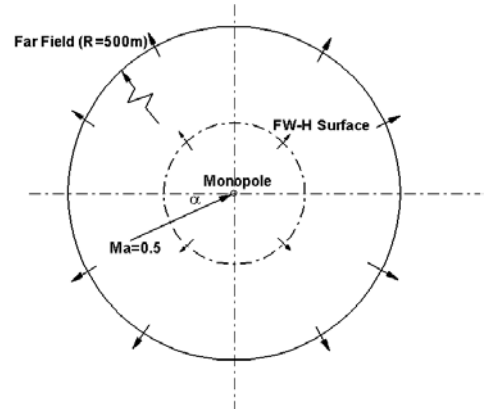
$$\rho' = \frac{p'}{c_0^2}$$

Figure 4. Schematic of a line monopole radiation.

The source terms in the FW-H integral are calculated over one period on the circular integration surface with the radius of $r = 1$ m for the case of $M = 0.5$, $\theta = 20°$, $A = 0.01 \text{ m}^2/\text{s}$ and $\omega = 3000 \text{ rad/s}$. With the near field perturbation variables on the integration surface, the far field acoustic pressure is predicted by the FW-H integral. The directivity and time history at a fixed observer are calculated and compared to the analytical solutions. The agreement shown in Figures 5 and 6 is excellent. The code for solving the FW-H integral is verified and will be used in Sec. IV to predict the far field noise generated by the flows around the various NACA airfoils (see table 1).
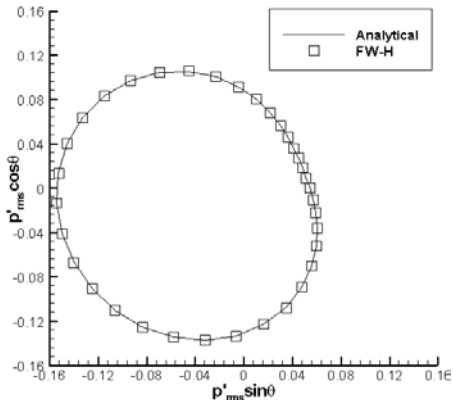

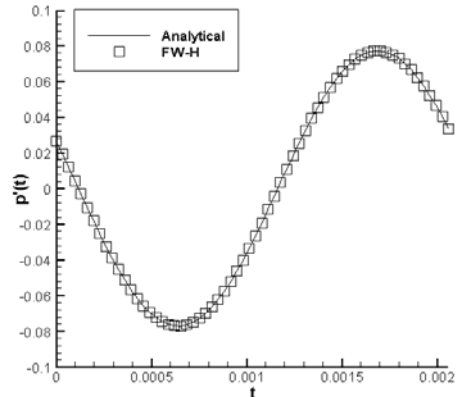Figure 5. Comparison of the far field directivity ($R = 500\,m$).

Figure 6. Time history comparison at an observer (500m, 0m).

IV. Results and Discussions

An unsteady flow simulation is carried out using the CFD solver described earlier for various symmetric and asymmetric airfoils (see Table 1). The freestream flow conditions shown in Figure 7 are used for all simulated airfoil cases. At the angle of attack 20° the flow around the airfoil is unsteady for all cases and is characterized by a time dependent behavior of the separation region around the airfoil. The statistics of the drag and lift coefficient is given in Table 2 for all cases. Results show that the fluctuations of the lift and drag coefficient for the cases of NACA 0006, 0009, 0012, and 2409 are much larger than those for the other airfoil cases. It is also noted from the table that a better aerodynamic performance with a moderate thickness is achieved not by producing more lift but by producing less drag for the symmetric airfoils. For the asymmetric airfoils, the aerodynamic performance improves as the maximum camber of the airfoil increases. The optimum position of the maximum camber seems to be around the center of an airfoil.
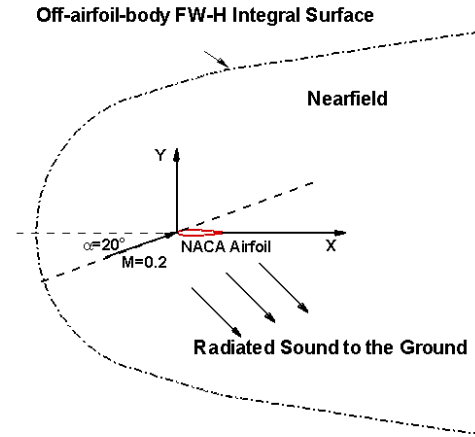

Figure 7. Schematic of the flow around an airfoil.

Table 2. Statistics of the unsteady lift and drag

00xx	Lift	Drag	LIFT_rms	Drag_rms	Freq. (Lift)	Drag/Lift
NACA 0006	0.9482	0.3693	0.066807	0.020971	104.5	0.3895
NACA 0009	0.8931	0.3595	0.067452	0.019763	104.5	0.4025
NACA 0012	0.8043	0.3256	0.044492	0.008228	115.0	0.4048
NACA 0015	0.7705	0.2256	0.012404	0.003959	141.6	0.2928
NACA 0018	0.8164	0.1791	0.005405	0.001791	165.6	0.2193
NACA 0024	0.8173	0.1568	0.007763	0.002296	180.5	0.1919
NACA 0030	0.7313	0.1658	0.021158	0.004735	168.8	0.2268
xx09						
NACA 2409	0.9879	0.3713	0.064773	0.018561	102.1	0.3759
NACA 4409	1.1038	0.341	0.027035	0.008601	116.2	0.3090
NACA 6309	1.2207	0.2661	0.020066	0.007874	133.4	0.2180
NACA 6409	1.1807	0.2753	0.014131	0.005835	126.1	0.2332
NACA 6609	1.1321	0.3526	0.013421	0.005577	109.4	0.3115
NACA 8409	1.3556	0.2653	0.018634	0.007754	132.4	0.1958
xx12						
NACA 2412	0.9145	0.2634	0.016909	0.006214	129.4	0.2881
NACA 4412	1.1047	0.2148	0.005937	0.002305	147.6	0.1945
NACA 6412	1.2757	0.2094	0.006891	0.002873	152.0	0.1641
NACA 8312	1.3741	0.2333	0.015281	0.006348	142.8	0.1698
NACA 8412	1.4249	0.2169	0.010965	0.004702	148.5	0.1523
NACA 8612	1.4669	0.2276	0.005544	0.002435	143.5	0.1552

The pressure coefficient distributions on the surface of an airfoil for all cases are shown in Figures 8 – 10. The results indicate a drastic decrease of $-c_p$ near the leading edge on the suction side of the airfoil surface and a smaller value of $-c_p$ near $x \to 0$ for the cases with higher lift and drag fluctuations. For the cases with lower lift and drag fluctuations, $-c_p$ reaches a value between 3 to 6 and then decreases gradually as x is increased. As a result of these two different characteristics in the pressure distributions, two
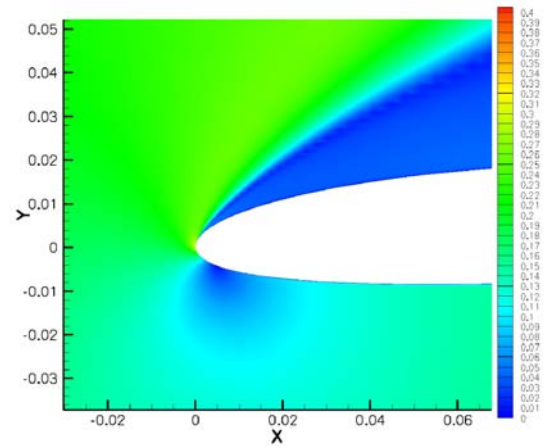
Figure 11. Averaged Mach number contours of the flow around the NACA 2409.
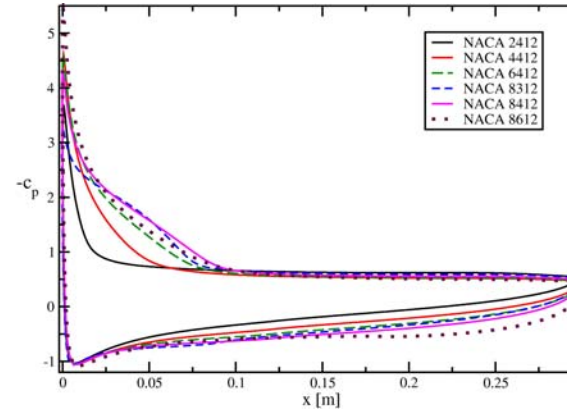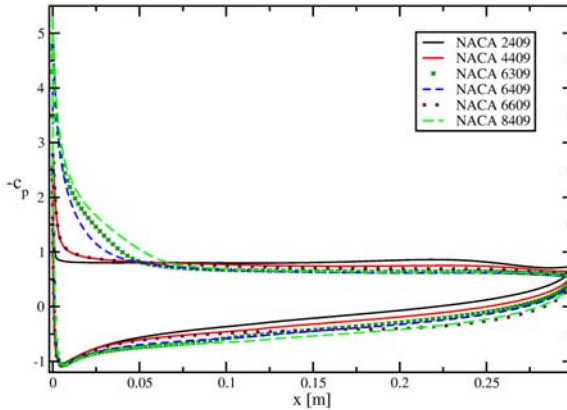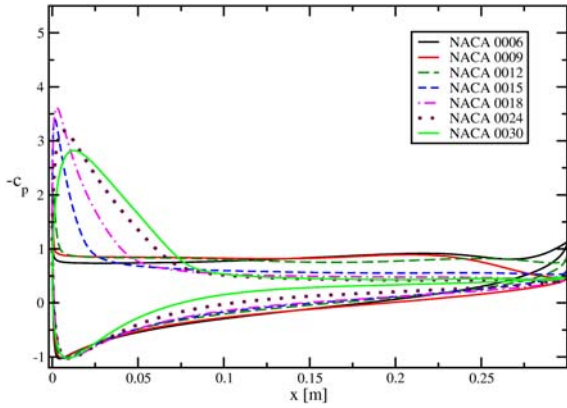
Figures 8 – 10. The pressure coefficient c_p on the surface of the airfoils.

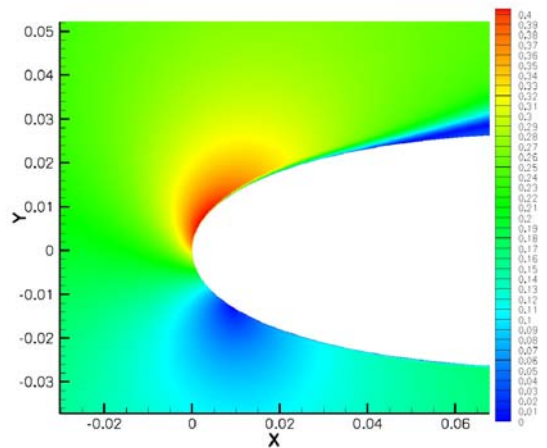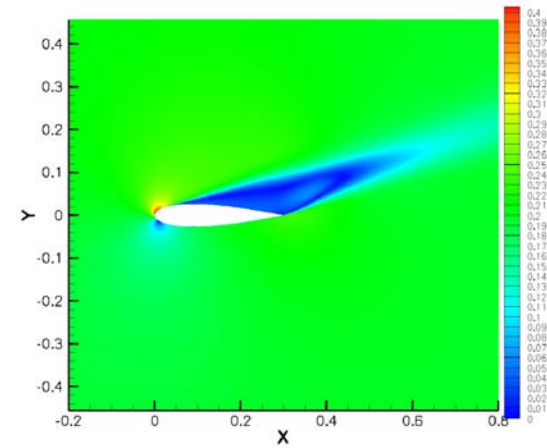Figure 12. Averaged Mach number contours of the flow around the NACA 0018.

American Institute of Aeronautics and Astronautics

different unsteady flow patterns around the airfoils are observed. In order to give a qualitative overview of the flow patterns around the airfoils, the averaged Mach number contours for the NACA 2409 (a typical case with higher lift and drag fluctuations) and NACA 0018 (a typical case with lower lift and drag fluctuations) are depicted in Figures 11 and 12, respectively. It is shown clearly from these figures that the location of the flow separation is different for the two cases, one with the flow separation right on the leading edge region (NACA 2409) and the other with the flow attached up to 10% of the chord length from the leading edge (NACA 0018). The separation right on the leading edge caused by the strong boundary layer eruption tends to result in an increase of the lift and drag fluctuations. Along with these Mach number contours, the instantaneous contours of the λ_2 criteria, which detect the main vortex structures, are shown in Figures 13 and 14 for both cases. A lower frequency of the vortex shedding with larger vortex structures is observed for the NACA 2409 and the opposite for the NACA 0018. As a result, the cases with higher lift and drag fluctuations have the lowest main propagation frequency (around 100 Hz). This can also be confirmed from the data in Table 2. The pressure perturbations for both cases are shown in Figures 15 and 16. As expected, the amplitude of the pressure perturbation $\Delta p'$ is much larger for the NACA 2409 ($\Delta p' = 40\,\text{Pa}$) than that for the NACA 0018 ($\Delta p' = 5\,\text{Pa}$). Furthermore, the sound radiation from the airfoil shows a dipole characteristics for both cases and the nonreflecting boundary conditions work very well in the simulations.
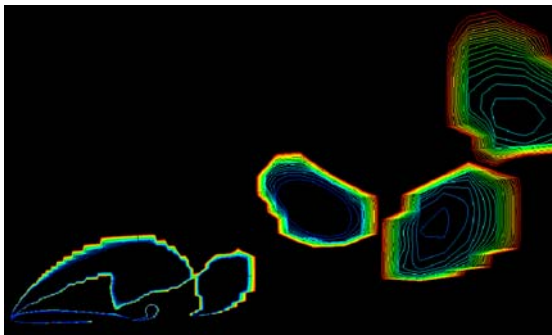

Figure 13. Instantaneous λ_2 criteria for detecting the main vortex structure of the NACA 2409.
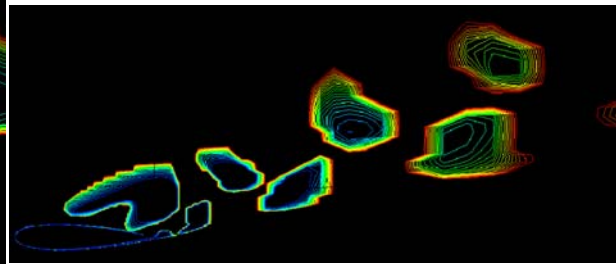

Figure 14. Instantaneous λ_2 criteria for detecting the main vortex structure of the NACA 0018.
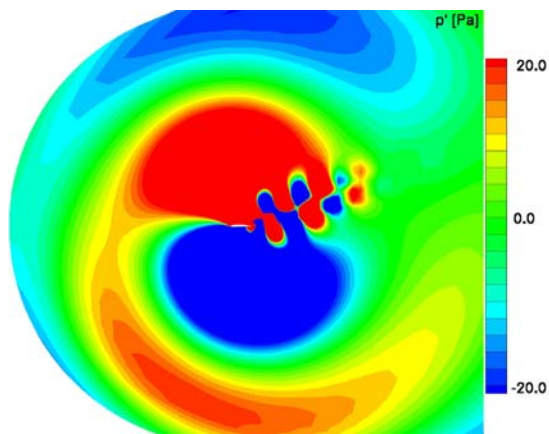

Figure 15. Instantaneous pressure perturbations of the NACA 2409 ($\Delta p' = 40\,\text{Pa}$).
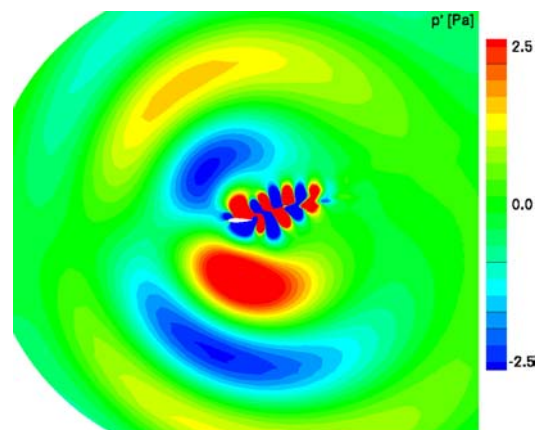

Figure 16. Instantaneous pressure perturbations of the NACA 0018 ($\Delta p' = 5\,\text{Pa}$).

To study the far field noise generated by the flows around the airfoils, a hybrid method that couples the CFD solver with the FW-H far field acoustic prediction is used. The FW-H integration surface is depicted in Figure 7. The perturbation and mean flow variables on the surface are obtained from the CFD simulations. Through the spectrum analysis of the perturbation variables, a main frequency can be found for each case. As an example, the pressure perturbations at four different locations on the integration surface for the NACA 0018 are shown in Figure 17. It can be seen that the pressure perturbations are nearly periodic with a frequency of $165.6\,\text{Hz}$. The FW-H equation in the frequency domain is then used to predict the far field noise. The quadrupole term is negligible in the current study due to its small contributions. The far field directivities ($R = 10\,\text{m}$) for the symmetric airfoils and the asymmetric airfoils of the NACA xx09 are shown in

Figure 17. Pressure perturbations at different locations on the FW-H integration surface.

Figures 18 – 19, respectively (unfortunately the unsteady flow variables on the integration surface for the NACA xx12 are not available at the moment due to an output error). In order to evaluate the overall far field noise level generated by the flows around these airfoils, the acoustic energy density is calculated and normalized by that of the reference case (NACA 0009) over the radiated region of $\pi \leq \theta \leq 2\pi$. The values of AED are given in Table 3. The results show that the noise generated by the thicker symmetric airfoils and the asymmetric airfoils with higher camber is much lower. Considering the unsteady flow patterns around the airfoils discussed earlier, the direct correlation between the far field noise and the level of the nearfiled unsteady flow fluctuations is confirmed.
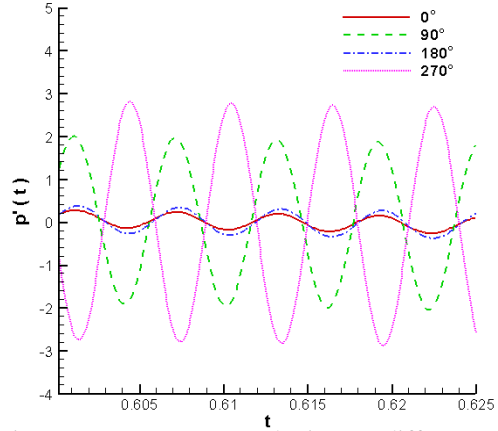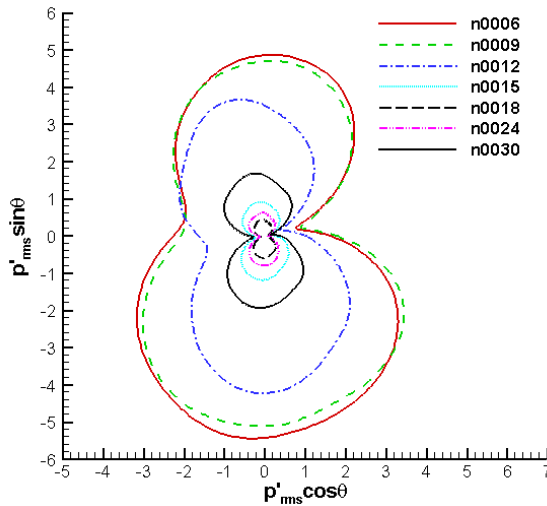

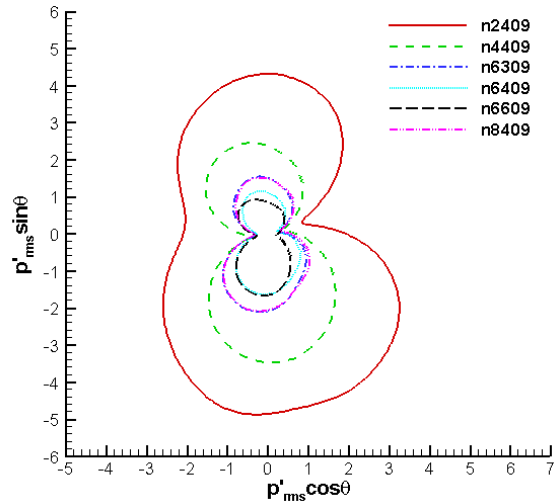Figure 18. Far field directivity patterns of the symmetric airfoils.

Figure 19. Far field directivity patterns of the asymmetric airfoils (NACA xx009).

In order to reveal the link between an airfoil shape characteristics and its combined aerodynamic and aeroacoustic performance, for all cases listed in Table 3, the following two objective functions are evaluated

$$\text{Obj}_1 = \alpha \frac{(C_d/C_l)}{(C_d/C_l)_{ref}} + (1-\alpha) \frac{AED}{(AED)_{ref}} \tag{5}$$

and

$$\text{Obj}_2 = \alpha \frac{(1/C_l)}{(1/C_l)_{ref}} + \beta \frac{C_d}{(C_d)_{ref}} + (1-\alpha-\beta) \frac{AED}{(AED)_{ref}} \qquad (6)$$

where α and β are the weighting parameters. The first objective function is formed by two terms, the aerodynamic factor term and the aeroacoustic factor term. These two terms are aimed to minimize the drag to lift ratio of an airfoil and the overall radiated noise in the directions of interest, respectively. The second objective function is formed by three terms. The aerodynamic factor is split into two terms, the lift term and the drag term. The aeroacoustic factor remains the same as it is given in the first objective function. As can be seen from Eqs. (5) and (6), these aerodynamic and aeroacoustic factors are normalized by the corresponding values of the

Table 3. Overall radiated noise level for various airfoils.

No.	Airfoil	$\sum_{\text{radiated to the ground}} {p'_{rms}}^2$	$\dfrac{\sum_{\text{radiated to the ground}} {p'_{rms}}^2}{\left(\sum_{\text{radiated to the ground}} {p'_{rms}}^2\right)_{ref}}$
1	N0006	3166.49	1.058478
2	N0009	2991.55	1
3	N0012	1493.25	0.499156
4	N0015	121.20	0.040514
5	N0018	27.17	0.009082
6	N0024	51.74	0.017295
7	N0030	319.47	0.106791
8	N2409	2642.80	0.883422
9	N4409	991.64	0.33148
10	N6309	381.86	0.127646
11	N6409	232.38	0.077679
12	N6609	200.43	0.066999
13	N8409	390.45	0.130518

reference case (NACA 0009). A change of the weighting factors, α and β, allows us to explore sensitivities of the objective functions to various weightings of the aerodynamic and aeroacoustic performance. The minimum value of the objective function, obj_1, and the corresponding case number are given in Figures 20 and 21 as a function of α. The optimum airfoils obtained from this objective function is the NACA 0018 or the NACA 0024 depending on the values of α. Evaluating the objective function, obj_2, the results given in Figures. 22 and 23 suggest that the optimum airfoils remain unchanged (NACA 0018 and 0024) if more weight is given to the drag term. However, when more weight is given to the lift term, the NACA 6409 and 8409 become optimum choices. Overall, the results show that the optimum airfoils are not overly sensitive to the choices of the weighting factors and the objective functions. It is worth a mention that the lower left triangular is the valid solution region where $\alpha + \beta \leq 1$.
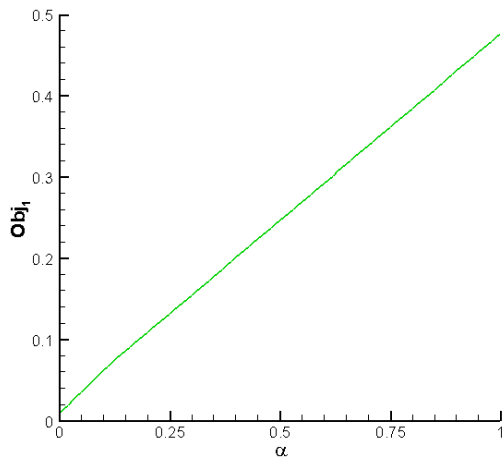

Figure 20. The objective function obj_1 as a function of weighting factor α.
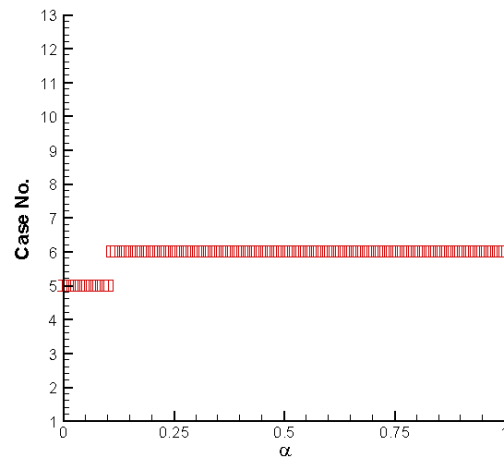

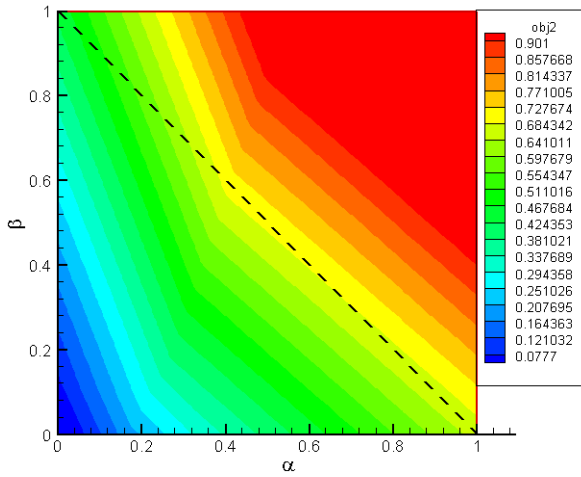Figure 21. The optimum cases obtained from the objective function obj_1.

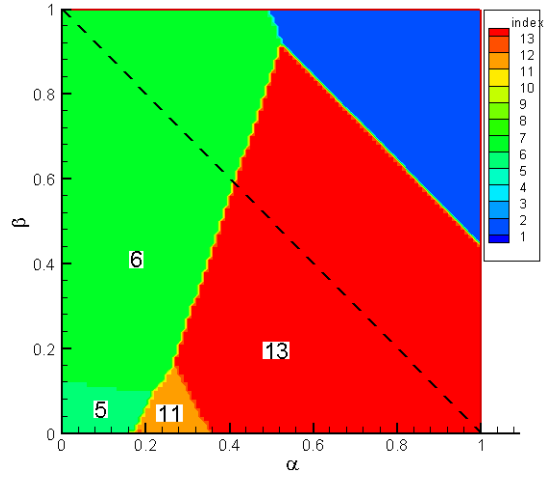Figure 22. The objective function obj_2 as a function of weighting factors α and β.

Figure 23. The optimum cases obtained from the objective function obj_2.

V. Conclusion

The aerodynamic and aeroacoustic performance of a series of NACA airfoils is analyzed. It is found that an airfoil with a moderate thickness (NACA0018 and 0024) has an optimum combined aerodynamic and aeroacoustic performance for the symmetric airfoils. For the asymmetric airfoils, the combined performance reaches its optimum for the airfoils with a relatively large maximum camber that is located at 40% of the chord length from the leading edge (NACA 6409 and 8409). The results provide the characteristics of an optimum airfoil that can be used to guide the selections of the geometric parameters and constraints in a fully automated airfoil aerodynamic and aeroacoustic design optimization. Since the design optimization of an airfoil is a very large computational problem (it could lead to an unrealistic demand on CPU time), proper and practical constraints that would not compromise the robustness and the computational efficiency of optimization is an essential for reducing the extent of human intervention needed during optimization.

Acknowledgements

References

[1]Jones, B. R., Crossley, W. A., and Lyrintzis, A. S., "Aerodynamic and Aeroacoustic Optimization of Airfoils via a Parallel Genetic Algorithm," *Journal of Aircraft*, Vol. 37, No. 6, Nov.-Dec. 2000, pp. 1088-1098.

[2]Nadarajah, S. K. and Jameson, A., "Optimal Control of Unsteady Flow Using a Time Accurate Method," AIAA-Paper No. 2002-5436.

[3]Huyse, L. and Lewis, R. M. "Aerodynamic Shape Optimization of Two-Dimensional Airfoils Under Uncertain Conditions," NASA/CR-2001-210648, ICASE Report No. 2001-1.

[4]Gano, S. E., Renaud, J. E. , Batill, S. M. and Tovar, A. "Shape Optimization For Conforming Airfoils," AIAA Paper No. 2003-1579.

[5]Song, W. and Keane, A. "A Study Of Shape Parameterization Methods For Airfoil Optimization," AIAA Paper No. 2004-4482.

[6]Xue, L., Entwicklung eines effizienten parallelen Lösungsalgorithmus zur dreidimensionalen Simulation komplexer turbulenter Strömungen, PhD Thesis Technische Universität Berlin, 1998

[7]Bogey, C. and Bailly, C., "Three-dimensional non-reflective boundary conditions for acoustic simulation: far field formulation and validation test cases," Acta Acoustica, vol. 88 (463—471), 2002

[8]Rung, T. and Thiele, F., "Computational Modelling of Complex Boundary Layer Flows," Proc. 9th Int. Symp. On Transport Phenomena in Thermal-Fluid-Engineering, Singapore, 1996

[9]Rung, T., Lübcke, H. and Thiele, F., "Universal wall-boundary conditions for turbulence-transport models," Zeitschrift für angewandte Mathematik und Mechanik, Vol. 81(1); pp. 1756-1758, 2000.

[10]Applin, Z.T., "Pressure distributions from subsonic test of a NACA 0012 semispan wing model," NASA Technical Memorandum 110148, Sep. 1995.

[11]Lockard, D. P., "An Efficient, Two-Dimensional Implementation of the Ffowcs Williams and Hawkings Equation," *Journal of Sound and Vibration*, 2000, Vol. 229 (4), pp. 897-911.

[12]Dowling, A.P. and Ffowcs Williams, J.E., "Sound and Sources of Sound," 1983, 207-208, Westergate: Horwood Publishing, chapter 9.